Boosting the Sensitivity of the Nanopore Field-Effect Transistor to Translocating Single Molecules

Anne S. Verhulst, Dino Ruić, Kherim Willems, and Pol Van Dorpe

***Abstract*—Nano-scaling of metal-oxide-semiconductor (MOS) field-effect transistors (FETs) is exploited to benefit the interdisciplinary field of single-molecule biosensing. While single-molecule DNA sequencing is done successfully by ionic current sensing through nanopores, the unambiguous characterization of more complex single biomolecules, such as fast translocating proteins, remains challenging with existing techniques. However, the nanopore-FET (NP-FET), a device with a nanopore embedded within the channel of the FET, is a promising new device detecting the motion of a molecule through the nanopore based on the transistor's electronic current. This nano-scale FET-based approach enables next-generation single-molecule sensing by offering larger signals and hence higher bandwidth, responding to a key challenge of detecting fast translocating molecules, and by offering denser electronic system packing and therefore more parallel sensing. However, the sensitivity of the nanopore-FET reported so far was limited to about 30%. In this paper, we show that the inherent potential of this hybrid nanofluidic-nanoelectronic device significantly exceeds the initial reportings by demonstrating sensitivity predictions up to 1000%. Our findings are supported with 3D nanofluidic-nanoelectronic open-source device simulations. Insight in the versatility of the device is provided through geometrical device optimization and demonstration that the device is sensitive to both positively and negatively charged molecules in both n- and p-channel FET configurations. These promising features, together with the immense expertise in MOS fabrication and scaling, offer a path to a highly parallelized and scalable sensor platform for genomics and proteomics.**

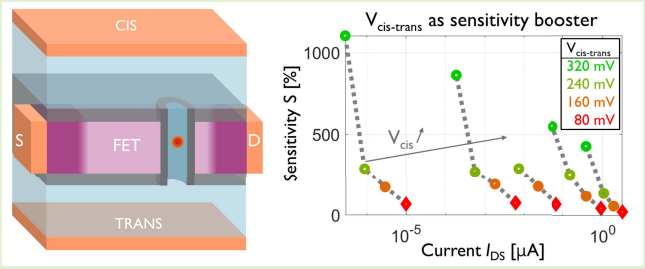

***Index Terms*—Nanopore, proteomics, single molecule, translocation.**

I. Introduction

DETECTION of single molecules is the pathway to further revolutionize the life sciences. Ever since the first single-molecule detection [1], the number of techniques capable of single-molecule sensing has increased and so did the number of applications benefiting from these scientific advances [2], [3]. Until recently, the two dominant single-molecule sensing techniques were fluorescence spectrocopy and force spectroscopy [4]. One of the major drawbacks of these techniques is the low throughput.

Nanopore-based detection is a more recent yet very promising third technique for single-molecule sensing [5]. With this technique, which is at the heart of state-of-the-art systems for DNA sequencing, the translocation of a single molecule through a nanopore is detected, based on measurements of the ionic current passing through the pore [6]–[12]. Nanopore-based sensing allows to take the first steps towards proteomics [13], [14], the stepping stone towards understanding cellular processes and hence disease development, a significantly more challenging task than DNA sequencing for several reasons. First, there is the lack of biochemical protein amplification methods [15]. Secondly, the compositional variation of proteins is larger, because they are built from 20 amino acid as opposed to the 4 bases that constitute DNA. Finally, limiting the speed with which individual molecules pass through the nanopore is key in ensuring a detectable signal. For DNA molecules a plethora of molecular machines, typically enzymes, are available to

Manuscript received January 18, 2022; accepted January 28, 2022. Date of publication February 7, 2022; date of current version March 14, 2022. This work was supported by the imec's Industrial Affiliation Program. The associate editor coordinating the review of this article and approving it for publication was Dr. Partha Bhattacharyya. *(Corresponding author: Anne S. Verhulst.)*

Anne S. Verhulst is with imec, 3001 Leuven, Belgium, and also with the Department of Electrical Engineering, KU Leuven, 3001 Leuven, Belgium (e-mail: anne.verhulst@imec.be).

Dino Ruić was with imec, 3001 Leuven, Belgium, and also with the Department of Physics and Astronomy, KU Leuven, 3001 Leuven, Belgium. He is now with Alphabet's X, Mountain View, CA 94043 USA.

Kherim Willems is with imec, 3001 Leuven, Belgium, and also with the Department of Chemistry, KU Leuven, 3001 Leuven, Belgium.

Pol Van Dorpe is with imec, 3001 Leuven, Belgium, and also with the Department of Physics and Astronomy, KU Leuven, 3001 Leuven, Belgium (e-mail: pol.vandorpe@imec.be).

Digital Object Identifier 10.1109/JSEN.2022.3149345

control (*i.e.*, reduce) the speed with which the DNA molecules pass through the pore [16]. However, such velocity-reduction mechanisms are not readily available for protein molecules. Detecting single proteins with nanopores therefore remains challenging.

Whereas to date biological nanopores still outperform their solid-state counterparts for DNA-based applications, the latter offer many advantages for more complex single-molecule sensing [17], [18]. For example, the size, shape, and surface properties of the solid-state pore can be readily adjusted to meet the needs required for optimal sensing of any given molecule, like *e.g.* a protein [19]. Also, the formation process of solid-state pores is not stochastic in time and in location, and the pores are physically and chemically more robust than their biological counterparts, enabling them to withstand *e.g.* larger applied voltages. It is, however, the more straightforward co-integration with electronic devices that makes switching to solid-state nanopores very attractive for single-molecule sensing [20]–[25].

A promising candidate within this category of electronic-current-based and nanopore-based sensing is the nanopore field-effect transistor (NP-FET), whereby a nanopore is embedded in the channel of a FET, such that a translocating molecule contributes to gating the FET and hence affects the FET's (electronic) current [26]–[31]. This hybrid nanofluidic-nanoelectronic device aims at the detection of single molecules which are translocating fast. The larger detection bandwidth is originating from the significantly larger electronic current used for sensing, as opposed to the ionic current, used within the biological-nanopore detection system. This larger electronic current is furthermore beneficial for the NP-FET's integration density, because of the smaller area of the required amplifiers and hence overall read-out circuitry. Finally, the parallelization of NP-FETs also looks inherently more optimistic than for biological-nanopore-based setups, because separate liquid reservoirs and individual liquid electrodes are no longer required [8], [9].

The NP-FET is especially interesting today, as the massive miniaturization effort over many decades has resulted in state-of-the-art metal-oxide-semiconductor FETs (MOSFETs) with gate lengths and body thicknesses below 20 nm, making them true nano-devices. The dimensions of these nanoelectronic devices are therefore aligned to the size of molecules of interest, like proteins, which opens up possibilities for enhanced molecular detection [32]. Together with the maturity of the silicon platform, with the promise of large-scale integrability of solid-state nanopores with on-chip electronics and with the promise of massive parallelism, the NP-FET is therefore up for a breakthrough in the field of single-molecule detection and in particular in proteomics. However, the predicted sensitivity S of the NP-FET, though being reasonable ($S \approx 20$ to 30%), is not splendid [30].

In this work, we show that the NP-FET, unlike many other bio-FETs [33], [34], has a unique booster parameter. In particular, the operating point of the NP-FET can be set independently from the effective voltage-change, sensed by the nanopore-gate of the NP-FET, upon a translocation event. This feature allows to boost the sensitivity of the NP-FET significantly to values up to $S = 1000\%$—without a clear upper limit—as our 3D hybrid nanofluidic-nanoeletronic device simulations show.

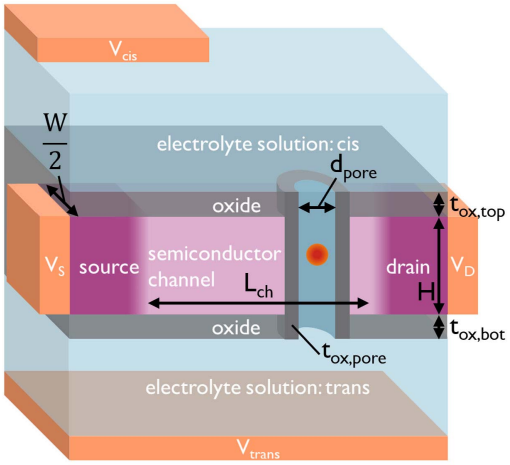

Fig. 1. Cross-sectional view of the 3D NP-FET (cross-sectional plane cuts the device symmetrically along the MOSFET channel length). The MOSFET has a uniform source and drain doping of 10^{20}cm^{-3} n-type or p-type doping for respectively n-channel or p-channel MOSFET). Towards the channel, this doping has a Gaussian profile with a variance of $\sigma = 4$ nm. The MOSFET channel has a uniform counter-doping of 10^{17}cm^{-3}. The channel length L_{ch} is defined as the distance between the source-channel and channel-drain junction. Note that the *cis* electrode is drawn small to better reflect an experimental setup, where the *cis* electrode typically is a probe inserted into the electrolyte.

We further increase the insight into the device, by unravelling the geometrical impact on the nanopore FET's sensitivity. We document the versatility of the device by showing that it can be used both in an n-channel and a p-channel configuration, and that it is sensitive to both positively and negatively charged molecules, although the sensitivity to positively charged molecules will typically be larger. Finally, we show that the sensitivity of the NP-FET is impacted by both the local charge as well as by the changes in effective gate voltage of the FET upon a translocation event.

II. Results and Discussion

A. Simulation and Structural Details

To investigate the promise of the NP-FET, 3D finite-volume simulations are performed [30], [35]–[37]. While Poisson's equation, which relates the charge density to the electrostatic potential variations, is solved for in the entire device (see Fig. 1 and App. A), the transport in the different regions of this hybrid nanofluidic-nanoelectronic device is governed by region-specific equations. In the semiconductor region of the MOSFET, the transport of electrons (for an n-channel FET) and holes (for a p-channel FET) is governed by the drift-diffusion equation. In the oxide regions, which are made of dielectric materials, no current flows. Transport in the (incompressible) fluidic regions is governed by the Nernst-Planck and the Navier-Stokes equations. Given the absence of pressure differences between the *cis* (*i.e.*, top) and *trans* (*i.e.*, bottom) reservoirs, the main driving force in the Navier-Stokes equation is an electric-field based body force [38], resulting in an electro-osmotic flow. Note that the presence of traps at

the semiconductor-oxide interface is taken into account as a generation-recombination term in the drift-diffusion model which contributes a charge density in Poisson's equation.

The NP-FET has four electrodes (see Fig. 1). In the fluid, there are the *cis* and *trans* electrodes. The fluid itself consists of water, a (low-mobility) buffer solution to fix the pH, and an electrolyte, typically a salt, to increase the fluid's electrical conductivity. These salt ions, upon applying a voltage difference between the two fluid electrodes, $V_{\text{cis-trans}} = V_{\text{cis}} - V_{\text{trans}}$, provide an observable electrical (ionic) current $I_{\text{cis-trans}}$, flowing from the *cis* reservoir through the nanopore to the *trans* reservoir. At the same time, the fluid represents the gate electrode to the FET, both as a top and bottom gate electrode, with as dielectric the top and bottom oxide respectively, and as an internal cylindrical gate electrode, with as dielectric the pore oxide. The other two FET electrodes are the source and the drain electrode. The voltages V_{G} (gate), V_{S} (source) and V_{D} (drain), applied to these three electrodes, determine the FET current I_{DS} flowing from drain to source. In the most sensitive NP-FET, the current I_{DS} dominantly responds to the internal cylindrical gate electrode, while the impact of the top and bottom gate electrodes is negligible.

The sensitivity $S_{loc,q}$ of the NP-FET to a molecule with charge q positioned at a location loc inside the nanopore is defined as:

$$S_{loc,q} = \frac{I_{\text{DS},loc,q} - I_{\text{DS,no molecule}}}{I_{\text{DS,no molecule}}} \cdot 100\%. \tag{1}$$

Upon moving through the nanopore (translocation), the molecule changes the ionic current but also the electrostatic potential along the nanopore. The latter represents the gate electrostatic potential and therefore affects the current through the FET.

B. Sensitivity Versus Subthreshold Swing

Typical sensitivities of about 20% have been achieved in previous predictive work [30]. To achieve these sensitivities, a nanoscale FET is required. This is dictated in the first place by the nanopore, which should have a diameter d_{pore} comparable to the size of the molecule passing through the pore to maximally affect the fluidic flow: $d_{\text{pore}} \leq 10$ nm. This diameter is representative for the effective gate length L_{G}. With such a short gate, the width of the FET has to be small as well, to maintain good electrostatic control over the channel [39], and hence to maximize the change in FET current upon a translocation event. Since the NP-FET is most comparable to 2 single-gate MOSFETs in parallel, the ratio of half the width $W/2$ to the gate length L_{G} (assuming a pore centered along the width of the FET) is preferable not more than $\frac{(W-d_{\text{pore}})/2}{L_{\text{G}}} \leq 0.4$ or equivalently $\frac{W-d_{\text{pore}}}{L_{\text{G}}} \leq 0.8$ [40]. The latter inequality is based on the assumption that, as in conventional MOSFETs, channel length L_{ch} and gate length are comparable. The gate of the NP-FET has, however, an unconventional structure and its length is smaller than the channel length. Therefore, the above inequality is to be used as a qualitative guideline only. The channel length L_{ch} should not be too long, to maximize the resistive change near the nanopore with respect to the total channel resistance. All other design parameters can be optimized for maximal electrostatic control of the gate over the channel as in conventional MOSFETs, *e.g.* the impact of the height H will be limited while ensuring a thin pore oxide $t_{\text{ox,pore}}$ is important to improve the control of the nanopore gate.

To maximize the sensitivity $S_{\text{loc},q}$, the optimal operation point of the FET has to be determined. Since the sensitivity represents a relative change in current, it is linked to the subthreshold swing (SS), which is defined as the gate-voltage shift required to induce a relative current change of one decade. In particular, if the molecule would induce a fixed (*i.e.*, independent of the transistor operation point) voltage shift $\Delta V_{\text{ch},q}$ in the nanopore at the location of the semiconductor channel and provided that the gate control occurs through the fluidic potential in the nanopore only, the following would apply (see also Ref. [33]):

$$\begin{aligned} S^{\text{SS}}_{\text{loc},q} &= \frac{10^{\Delta V_{\text{ch},q}/\text{SS}} \times I_{\text{DS,no molecule}} - I_{\text{DS,no molecule}}}{I_{\text{DS,no molecule}}} \cdot 100\% \\ &= \left(10^{\Delta V_{\text{ch},q}/\text{SS}} - 1\right) \cdot 100\%. \end{aligned} \tag{2}$$

Equation 2 indicates that the highest sensitivity is obtained for the smallest value of SS. The most favorable operation condition of the FET is therefore operation near or below threshold, for an architecture that has tight gate control over the channel and a low trap density at the oxide-semiconductor interface. There is of course some impact of the transistor operation point on the fluidic flow and hence on the value of $\Delta V_{\text{ch},q}$. At the same time, the voltage shift in the nanopore is not fixed over the entire height of the semiconductor channel and this non-uniform gating affects the FET current differently in different operating regimes. Finally, the FET is also locally affected by a direct action of molecular charge (the latter impact will not be investigated in detail in this manuscript, as there is no design parameter identified to enhance the molecular charge action). Therefore, Eq. 2 will only approximately hold, yet the qualitative trend of improved sensitivity for smaller values of SS is expected to be observable.

3D hybrid nanofluidic-nanoelectronic device simulations have been executed to document the NP-FET performance and its dependence on geometrical parameters and operating voltage. Fig. 3(a)-(b) and Fig. 7(a) show the open-pore I_{DS}-V_{cis} characteristics of the different architectures in Fig. 2. Architectures `#1`, `#2` and `#3` show the impact of a variation in channel length L_{ch} (70, 50 and 30 nm, respectively). As expected, the current becomes larger and more difficult to turn off as L_{ch} decreases, because the source-drain electrostatic barrier becomes smaller and the gate looses electrostatic control over the channel, as discussed before. The better SS of architecture `#1` versus `#2` or `#3` is quantified in Fig. 3(c). Decreasing the channel width W_{ch} (`#3` to `#4`, 40 nm to 25 nm, resp.) decreases the current, as the cross-sectional area between source and drain decreases, and improves SS, due to the better electrostatic control of the gate. The I_{DS}-V_{GS} characteristics of `#4` are comparable to the ones of `#2`, as they have about the same $W_{\text{ch}}/L_{\text{ch}}$ ratio. Decreasing the pore diameter in the fluid $d_{\text{pore,fluid}}$ (`#4` to `#5`, 6 nm to 5 nm, resp.) or increasing the thickness of the top

NP-FET dimension	#1	#2	#3	#4	#5	#6	#7	#8
L_{ch}	70 nm	50 nm	30 nm	30 nm	30 nm	30 nm	30 nm	60 nm
W_{ch}	40 nm	40 nm	40 nm	25 nm	25 nm	25 nm	25 nm	60 nm
$d_{pore,fluid}$	6 nm	6 nm	6 nm	6 nm	5 nm	5 nm	5 nm	5 nm
$t_{top,ox}$	10 nm	10 nm	10 nm	10 nm	10 nm	30 nm	10 nm	10 nm
$t_{pore,ox}$	2 nm	2 nm	2 nm	2 nm	2 nm	2 nm	3 nm	2 nm

Fig. 2. Details of the NP-FET architectures studied. For all architectures, the applied voltages are $V_{DS} = V_D = 100$ mV and $V_{cis\text{-}trans} = 80$ mV, the channel height is $H_{ch} = 30$ nm, the bottom oxide thickness is $t_{bottom,ox} = 10$ nm, traps are present at the semiconductor-oxide interface with a surface trap density of 10^{11} cm^{-2}, the diameter of the molecule is $d_{molecule} = 3$ nm, the relative permittivity of the molecule is $\epsilon_{r,mol} = 2$, the (uniformly distributed) charge of the molecule is 10 q_e, the pH of the fluid is 4, the salt concentration is 1 mM NaCl, the silanol surface density is 4.8×10^{13} cm^{-2} (whereby the corresponding negative charge-density is pH-dependent). Note: similar or identical colors are used to highlight the parameter(s) that are different in two different architectures (orange indicates that architecture #5 is identical to architecture #4 except for the pore diameter in the fluid). This color is then also used for the electrical characteristics of the architecture with the largest architecture number (*e.g.* orange curves in Fig. 3 for architecture #5).

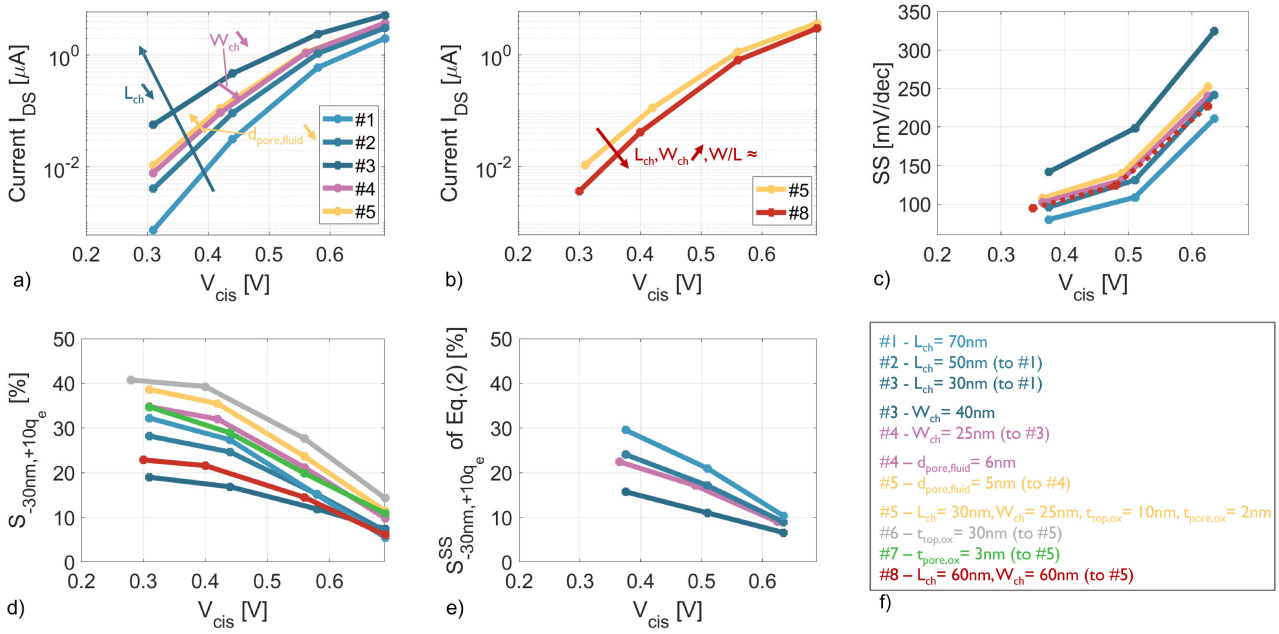

Fig. 3. Simulated electrical characteristics and sensitivity of the NP-FET architectures detailed in Fig. 2 at $V_{DS} = 100$ mV and $V_{cis\text{-}trans} = 80$ mV: (a)-(b) I_{DS}-V_{cis} characteristics of the NP-FETs with an open pore (no molecule); (c) SS-V_{cis} characteristics corresponding to (a)-(b), with $SS = \frac{dV_{GS}}{d\log_{10} I_{DS}}$; (d) Sensitivity versus V_{cis} according to Eq. 1; (e) Sensitivity versus V_{cis} according to Eq. 2 for architectures #1–4 with a realistic (based on 3D simulations) voltage shift $\Delta V_{ch,+10\,q_e} = 9$ *mV*. (f) The key architecture features of Fig. 2 are repeated here for ease of comparison.

oxide $t_{top,ox}$ (#5 to #6, 10 nm to 30 nm, resp.) does not affect the open-pore I_{DS}-V_{GS} characteristics, but will have an impact on the sensitivity of the NP-FET, as will be discussed later. Increasing the pore oxide thickness $t_{pore,ox}$ (#5 to #7, 2 nm to 3 nm, resp.), with the dominant gate action of the FET via the pore, increases SS somewhat (see Fig. 7(b)) but this change is hardly observable in the I_{DS}-V_{cis} characteristics (see Fig. 7(a)). Finally, an increase in both L_{ch} and W_{ch} with roughly the same ratio (#5 to #8) does not affect the I_{DS}-V_{GS} very much, but will have an impact on the sensitivity, as will be discussed next.

The sensitivity of each NP-FET to the translocation of a spherical molecule, with uniformly distributed positive charge of 10 q_e, is shown in Fig. 3(d) as a function of V_{cis}. The sensitivity value is calculated according to Eq. 1 with blocked-pore current values extracted from 3D simulations with a molecule positioned centrally in the pore at the height of the channel-to-bottom-oxide interface (the plane of the channel-to-top-oxide being the reference plane). This location has been shown to be the location of highest sensitivity [30]. As expected from Eq. 2, the sensitivity increases as the transistor is operated more in subthreshold, where the SS is the lowest. For architectures #1 to #3, the change in sensitivity with decreasing L_{ch} can be linked to their SS value. Decreasing W_{ch} enhances the efficiency of the molecular charge in turning on the FET (a proportionally larger volume is impacted in narrower devices) and increases nanopore-oxide gating with respect to top- and bottom-oxide gating. Therefore the sensitivity of architecture #4 increases over architecture #2, despite the nearly identical I_{DS}-V_{cis} characteristics. Decreasing the pore diameter $d_{pore,fluid}$ (#4 to #5) results in a larger local fluidic resistance in the pore around the molecule. For a molecule at height −30 nm (referenced to the top-oxide-semiconductor interface), the potential along H_{ch} is therefore closer to V_{cis}

in architecture #5 and hence $S_{-30\text{nm},10q_e}$ increases. Increasing $t_{\text{top,ox}}$ (#5 to #6) gives a lower reference current $I_{\text{DS,no molecule}}$ while the current for a blocked pore is comparable, hence the sensitivity increases further. The impact of increasing $t_{\text{pore,ox}}$ (#5 to #7) on the sensitivity is mostly explained by the slightly lower SS values. Finally, an increasing W_{ch} (#5 to #8) decreases the efficiency of the molecular charge in turning on the FET and decreases the nanopore-oxide gating versus the top- and bottom-oxide gating (see #2 to #4 too). Therefore, the sensitivity decreases despite the comparable I_{DS}-V_{cis} characteristics.

The expected sensitivity based on SS values only is displayed in Fig. 3(e) for architectures #1–4. The figure displays the results of Eq. 2, which assumes that the only impact of the molecule is a fixed voltage shift in the nanopore ($\Delta V_{\text{ch},10q_e} = 9$ mV is used, based on simulation data). Qualitatively, Fig. 3(d) and (e) are similar. However, the local impact of the charge on the FET gating and therefore on the sensitivity is not captured in Eq. 2, which results in deviations, particularly in architecture #4.

For the architectures #5 and #8, the performance of an NP-FET based on a p-channel FET (opposite doping type in source, drain and channel compared to n-channel FET) is also determined (see App. C). The simulations show that similar sensitivities are achieved with both FET configurations.

C. The Nanopore Analyzed

The impact of the molecule on the fluidic transport is documented in Fig. 4 for achitecture #8. In the absence of a molecule, the negative surface charge density at the pore oxide (due to the deprotonation of the surface silanol groups) enhances and depletes respectively the cation and anion concentrations inside the pore with respect to the external reservoirs (see Fig. 4(a)). In the presence of a positively charged ($10q_e$) molecule at a distance of 10 nm from the *trans* reservoir, the ion concentrations locally change again, whereby the cation concentrations decrease (as they are repelled by the positive charge) and the anion concentrations increase. At 10 nm distance from the molecule, the molecular charge is fully screened and the concentrations have resumed the values they would have in the absence of a charged molecule.

At an applied bias of $V_{\text{cis-trans}} = 80$ mV, the Na^+ and H^+ ion current densities are dominant (see Fig. 4(b)) and nearly equal, since the H^+ mobility is roughly a factor of 10 larger than the Na^+ mobility. The presence of a positively charged molecule decreases the total current density, because the drop in cation concentration locally around the molecule increases the electrical fluidic resistance. Detailed investigation shows that at the pore entrances, there is both a strong drift and diffusion component to the current density, while at the inside of the pore (more than 10 nm away from the pore entrances or from a molecule) there is only a drift component. Along the entire pore, the convection current is very small for the given operating conditions and its contribution can therefore be neglected. Note that the local variation in current density at the location of the molecule reflects the dependence of the current density on the proximity of the molecule (the total ion current through the nanopore is constant at each cross section since steady-state solutions are solved for).

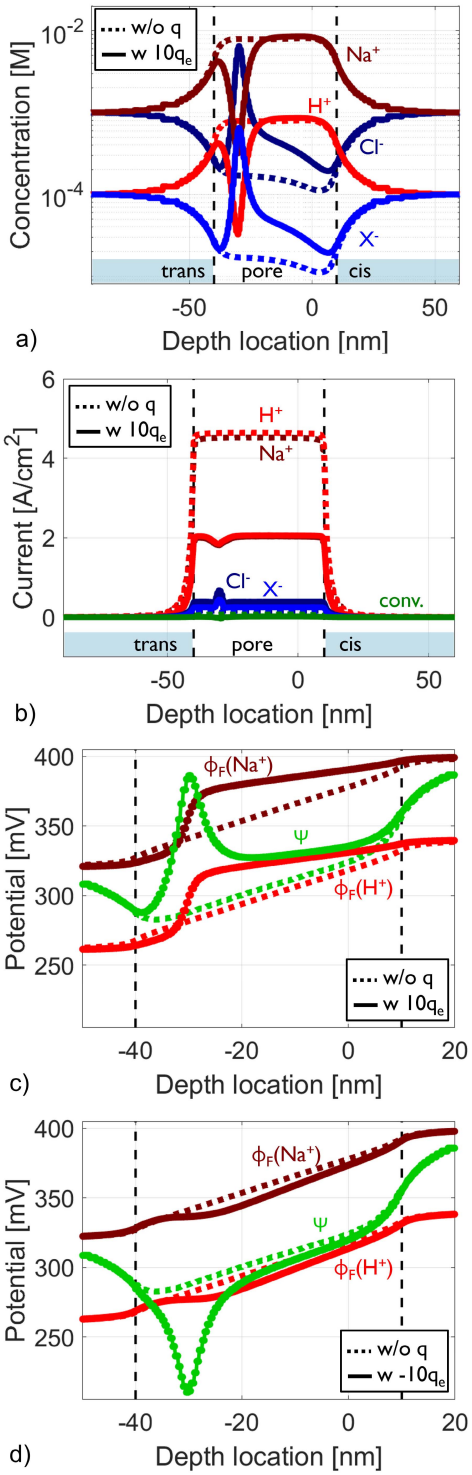

Fig. 4. Fluidic transport for architecture #8 with (solid) or without (dashed) the presence of a charged molecule at a depth of −30 nm for $V_{\text{cis-trans}} = 80$ mV and $V_{\text{cis}} = 400$ mV: (a) ion concentrations; (b) ion drift-diffusion current densities and total convection current density; (c) electrostatic (ψ) and electrochemical (ϕ_F) potential of H^+ and Na^+ with a *positively* charged molecule (+10 q_e) and (d) with a *negatively* charged molecule (−10 q_e). The data correspond to the values on a straight line at 2 nm distance from the center of the pore. Note: X^- represents the ensemble of all molecules which released H^+.

To analyze the change in gate action for the NP-FET dependent on the presence or absence of a charged molecule, the electrostatic potential together with the electrochemical potential of the dominant ion species is shown in Fig. 4(c) for a positively charged molecule and in Fig. 4(d) for a negatively charged molecule. In the absence of a molecule, the electrostatic potential changes rather linearly along the pore. A positively charged molecule causes a larger fluidic resistance at the location of the molecule, and hence a more gradually changing electrostatic potential in the remaining part of the pore. The electrostatic potential in the pore is therefore affected in two ways: on the one hand, the electrostatic potential with a positively charged molecule at a depth of −30 nm is more positive in the section of 0 nm depth to −20 nm depth than without molecule due to the changes in relative fluidic resistance (*i.e.*, resistive divider effect), on the other hand, the positive charge creates a local increase in electrostatic potential towards more positive values. Both effects increase the FET current compared to when no molecule is present. For a negatively charged molecule, which locally decreases the fluidic resistance, the change in electrostatic potential due to relative changes in fluidic resistance is more limited, so the dominant impact on the electrostatic potential, for the operating conditions as simulated in Fig. 4(d), is due to the local impact of the molecular charge. A more detailed description of the fluidic transport with a negatively charged molecule is provided in App. D where Fig. 9(c) illustrates the larger sensitivity of the NP-FET to positively charged molecules as compared to negatively charged molecules. Note that this larger sensitivity is linked to the negative silanol charge density and therefore, it is not an inherent feature of the NP-FET.

D. Sensitivity Booster

To increase the sensitivity further, the data in Fig. 4(c) suggest that the NP-FET, unlike many other bio-FETs, has a unique booster parameter. Upon increasing $V_{\text{cis-trans}}$, the average electrostatic potential value inside the pore along the semiconductor channel in the presence of a positively charged molecule, will deviate more and more from the average electrostatic potential value inside the open pore. Unlike a typical bio-FET, for which an increase in $V_{\text{cis-trans}}$ increases both the signal of interest and the reference signal, such that the sensitivity remains unchanged (see Eq. 1), the NP-FET allows one to set the reference FET current (*i.e.*, when no molecule is present) through the average value of the voltages V_{cis} and V_{trans}. The reference FET current value can therefore be decoupled from $V_{\text{cis-trans}}$. An increase of the average electrostatic potential translates in an exponential increase in the current when the FET is operated in subthreshold and hence an exponential increase in sensitivity (see Eq. 2). In strong inversion, the boost is more modest, starting from a linear increase in current with gate voltage change around threshold towards very small increases as the FET is operated more strongly in inversion. These assessments are qualitative only, as the sensitivity will also be impacted by the local charge, as well as by the (molecule-independent) gating through top and bottom oxide. To make a quantitative assessment, 3D simulations are required.

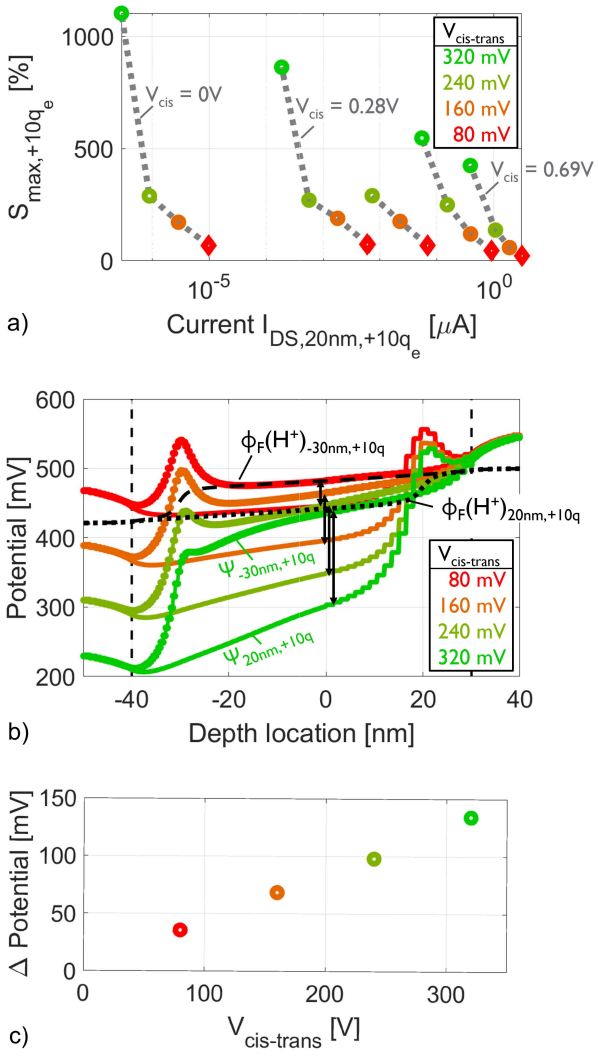

Fig. 5. Impact of increasing $V_{\text{cis-trans}}$ for architecture #6: (a) increase in maximum sensitivity for $V_{\text{cis}} = \{0,0.28,0.40,0.56,0.69\}$ V; (b) increase in electrostatic potential (ψ) difference for a positively charged molecule at a depth of $loc = -30$ nm (top curve) versus $loc = +20$ nm (bottom curve) with $V_{\text{cis}} = 0.56$ V; (c) difference in electrostatic potential between the top and bottom curve in (b) at a depth of $loc = 0$ nm (corresponding to the length of the black arrows in (b)). In (b), the electrochemical potential (ϕ_F) of H^+ is shown for $V_{\text{cis-trans}} = 80$ mV, illustrating the blocking impact of the molecule. The data in (b) correspond to the values on a straight line at 2 nm distance from the center of the pore.

The sensitivity boost of the NP-FET is illustrated in Fig. 5(a) with 3D hybrid nanofluidic-nanoelectronic device simulations. The sensitivity displayed is not the default sensitivity, which is determined with respect to the reference signal in the absence of a molecule (see Eq. 1), rather it is the maximum sensitivity, which captures the difference between the largest and the smallest FET current as the molecule translocates:

$$S_{\max,q} = \frac{I_{\text{DS},loc.max,q} - I_{\text{DS},loc.min,q}}{I_{\text{DS},loc.min,q}} \cdot 100\%. \qquad (3)$$

For architecture #6 (Fig. 5), $loc.max = -30$ nm and $loc.min = +20$ nm. Details of the fluidic transport with a

charged molecule at the top of the pore, similar to architecture #6 with $loc.min = +20$ nm, are provided in App. E including sensitivity predictions. Fig. 5(a) shows that similar to Fig. 3(c), the sensitivity is larger as the FET is operated more in subthreshold (threshold voltage $V_T \approx 0.5$ V). As expected, increasing $V_{\text{cis-trans}}$ improves the sensitivity more than linearly. Impressive sensitivity values up to 1000% are predicted for $V_{\text{cis-trans}} = 320$ mV. Larger $V_{\text{cis-trans}}$ values have not been simulated due to numerical reasons (*i.e.*, lack of convergence), but it is clear that the NP-FET has the potential for even larger sensitivities.

The electrostatic potential profile close to the nanopore edge is shown in Fig. 5(b). As is illustrated for a depth of 0 nm (see black arrows, also plotted explicitly in Fig. 5(c)), the difference in electrostatic potential as the molecule translocates from +20 to −30 nm increases with increasing values of $V_{\text{cis-trans}}$ and is therefore supporting the observed boost in sensitivity in Fig. 5(a). The electrochemical potential difference of H^+ is shown too for $V_{\text{cis-trans}} = 80$ mV. It illustrates the local blocking impact of the molecule in the nanopore.

The sensitivity of the NP-FET can be further increased by replacing the conventional MOSFET with a steep-slope FET (SS-value < 60mV/dec), *e.g.* a tunnel-FET or a steep-slope ferroelectric FET [41]–[43], such that the FET current changes more strongly for the same effective gate voltage change occuring during a translocation event (see Eq. 2) [33]. Note, however, that operation in subthreshold at lower current levels, also lowers the maximum bandwidth of the FET.

III. Conclusion

The nanopore-FET is a nanofluidic-nanoelectronic device, which is only feasible because of state-of-the-art sub-50 nm FET processing capabilities, allowing the integration of a sub-10 nm diameter pore in a sub-50 nm wide FET. This single-molecule sensing FET has a unique booster parameter, unlike many other bio-FETs. The operating point of the NP-FET can be set by the average value of V_{cis} and V_{trans}, independent of the value of $V_{\text{cis-trans}}$. Increasing the value of the latter parameter therefore boosts the sensitivity of the NP-FET enormously: sensitivity values of 1000% have been demonstrated via 3D hybrid nanofluidic-nanoelectronic device simulations, but there is no hard upper limit to the achievable sensitivity.

Details of the NP-FET behavior have been documented. In particular, it has been shown that the NP-FET can operate with both an n-channel and a p-channel configuration. Furthermore, due to the typically negative silanol surface charge density at the pore oxide, the NP-FET is more sensitive to molecules with a positive charge than to molecules with a negative charge. Finally, the sensitivity is impacted by both the average change in electrostatic potential along the nanopore at the height of the FET's channel, as well as by the local impact of the charge of the molecule on the FET's channel.

Our findings therefore motivate further research to unravel the full potential of the NP-FET. In particular, the sensitivity to larger (real) molecules needs to be studied as well as the expected noise and hence the achievable signal-to-noise ratio of a complete NP-FET system, including read-out circuitry. In such a more complete study, additional sensitivity boosters, such as replacing the conventional FET with a steep-slope FET, should be included.

Appendix A
Methods

The 3D hybrid nanofluidic-nanoelectronic device simulations are performed with a finite-volume implementation in OpenFoam v1812 [35]. A structured mesh consisting of rectangular volumes is used. The maximal mesh spacing is about 3 nm, with a graded meshing down to mesh spacings of 0.2 nm. The latter is used in regions where large variations are expected, *e.g.* around the nanopore.

Before starting the simulation, the doping profile in source, drain and channel region of the semiconductor are specified by the user. Furthermore, the trap density at the semiconductor-oxide interface is defined, as well as the silanol density at the oxide-fluid interface.

The self-consistent simulation procedure is outlined in the flowchart of App. Fig. 6. The procedure starts with initializations. First the electrostatic potential Ψ is initialized in the entire structure, whereby its value at the *cis* electrode and at the *trans* electrode is based on the externally applied voltage to these electrodes. In the semiconductor, initialization of the electrochemical potential Φ_F of the relevant carrier (electron or hole) is done, whereby its value at the source electrode and at the drain electrode is based on the externally applied voltage to these electrodes. In the fluid, initialization of the various ion concentrations $c_{\{Na^+,Cl^-,H^+,X^-\}}$ is done, whereby the value at the cis electrode and at the *trans* electrode is based on the user-specified values at these electrodes. Note that X^- represents the total of all anions in the fluid, except for Cl^-. Finally, the initialization is completed by calculating the missing value of $c_{\text{electron or hole}}$ in the semiconductor and the missing value of Φ_F for each ion in the liquid based on the following equation:

$$c = c_0 \exp \frac{z\,(\Phi_F - \Psi)}{V_{\text{th}}}, \tag{4}$$

with c_0 a material-dependent intrinsic concentration, z the number (including sign) of unit charges of the carrier or ion considered, and $V_{\text{th}} = \frac{kT}{q}$ the thermal voltage (with k the Boltzmann constant, T the temperature and q the unit of charge).

Next, the self-consistent loop starts. First a new value for Ψ is determined based on its initial value and an application of Newton's method to the Poisson Equation:

$$\nabla \cdot \left[\epsilon_0 \epsilon_r\,(\vec{r})\,\nabla\Psi\,(\vec{r})\right] = -\rho\,(\vec{r})\,, \tag{5}$$

with ϵ_0 the dielectric constant of vacuum and $\epsilon_r\,(\vec{r})$ and $\rho\,(\vec{r})$ respectively the relative dielectric constant and the charge density at every location in the system. In a next step, the drift-diffusion charge current density J_{DD} is determined for the relevant carrier in the semiconductor with a Scharfetter-Gummel discretization [44] based on the following equation:

$$\vec{J}_{DD}\,(\vec{r}) = -q\,\mu_n n\,(\vec{r})\,\nabla\Phi_{F,n}\,(\vec{r}) - q\,\mu_p p\,(\vec{r})\,\nabla\Phi_{F,p}\,(\vec{r}), \tag{6}$$

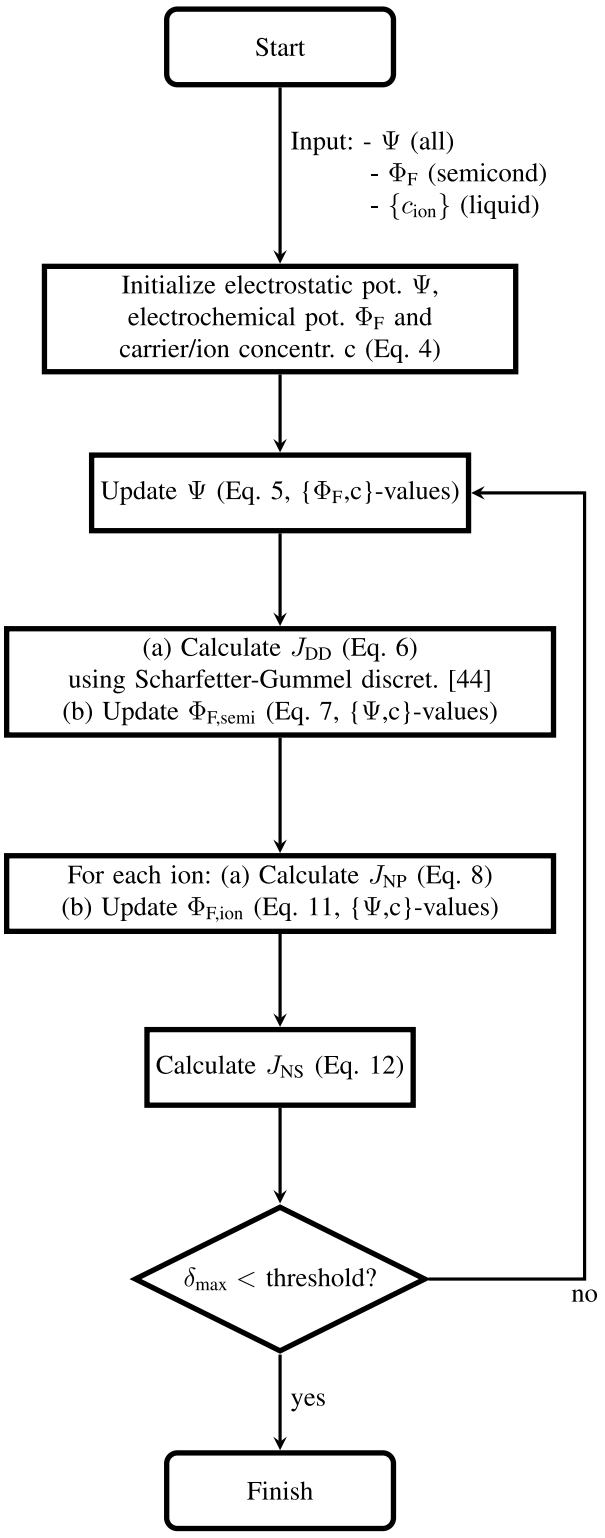

Fig. 6. Self-consistent simulation procedure.

with μ_n the electron mobility, n the electron density, μ_p the hole mobility and p the hole density. This drift-diffusion current value is then used to determine a new value for Φ_F in the semiconductor based on its initial value and an application of Newton's method to the current continuity equation in the semiconductor:

$$\nabla \cdot \vec{J}_{DD}(\vec{r}) = 0. \tag{7}$$

Note that the Caughey-Thomas mobility model is implemented in the semiconductor region, providing both a concentration- and a field-dependent mobility, the latter reflecting velocity saturation [45].

The same steps are then applied to the liquid, where now the Nernst-Planck equation is used to determine the charge current density contribution of each ion { Na^+, Cl^-, H^+ and X^+}:

$$\vec{J}_{NP,ion}(\vec{r}) = z_{ion} F \left[-\mu_{ion} c_{ion}(\vec{r}) \nabla \Phi_{F,ion}(\vec{r}) + \vec{u}(\vec{r}) c_{ion}(\vec{r}) \right], \tag{8}$$

with

$$\nabla \Phi_{F,ion}(\vec{r}) = \nabla \Psi(\vec{r}) + kT/(q z_{ion} c_{ion}) \nabla c_{ion}(\vec{r}), \tag{9}$$

$$D_{ion} = \mu_{ion}\, kT/(q z_{ion}), \tag{10}$$

with F the Faraday constant, μ_{ion} the ion mobility, $\vec{u}$ the fluid velocity and D_{ion} the ion diffusivity. A concentration-dependent mobility is implemented for Na^+ and Cl^-, while the mobility of H^+ and X^- is taken fixed at $\mu = 50 \times 10^{-4} cm^2 \cdot V^{-1} \cdot s^{-1}$. The ion current value of Eq. 8 is then used to determine a new value for $\Phi_{F,ion}$ based on its initial value and an application of Newton's method to the current continuity equation in the fluid:

$$\nabla \cdot \vec{J}_{NP,ion}(\vec{r}) = 0, \tag{11}$$

assuming an incompressible fluid. Finally, the steady-state Navier-Stokes equation is used to update the fluid velocity:

$$\nabla \cdot (\rho \vec{u} \otimes \vec{u}) - \mu_{fluid} \nabla \cdot (\nabla \otimes \vec{u}) = -\nabla p + \vec{f}, \tag{12}$$

with μ_{fluid} the fluid dynamic viscosity (which is assumed to be constant) and with the body force $\vec{f}$ given by:

$$\vec{f} = -F \nabla \Psi \sum_{ion} z_{ion} c_{ion}. \tag{13}$$

After this calculation, there is a convergence check point: if the maximum of all registered adjustments to electrostatic and electrochemical potential is smaller than a predefined threshold (*i.e.*, if the convergence criterion is met), the simulation finishes. If convergence is not reached yet, a new loop is started by first fine-tuning Ψ again and then Φ_F as shown in Fig. 6.

Appendix B
Characteristics of NP-FET Archs. #5 to #7

Fig. 7(a) shows the open-pore I_{DS}-V_{cis} characteristics of the architectures #5 to #7, described in detail in Fig. 2. The corresponding SS values are displayed in Fig. 7(b). As can be seen, the electrical characteristics are nearly coinciding, yet as discussed in the main manuscript, the sensitivity of the different architectures differs (see Fig. 3(d)).

Appendix C
N-Channel Versus p-Channel NP-FET

In a p-channel FET, there is opposite doping type compared to an n-channel FET in source, channel and drain (respectively p-type, n-type and p-type) and the device current is determined by the hole mobility instead of by the electron mobility,

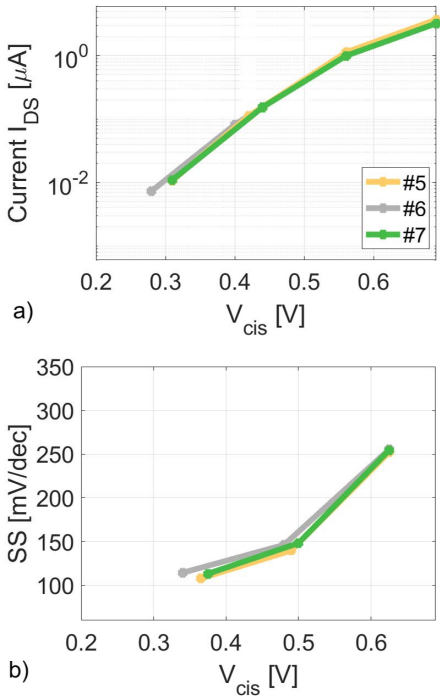

Fig. 7. Simulated electrical characteristics of the NP-FET architectures #5 to #7, detailed in Fig. 2, at $V_{DS} = 100$ mV and $V_{cis\text{-}trans} = 80$ mV: (a) I_{DS}-V_{cis} characteristics of the NP-FETs with an open pore (no molecule); (b) SS-V_{cis} characteristics corresponding to (a).

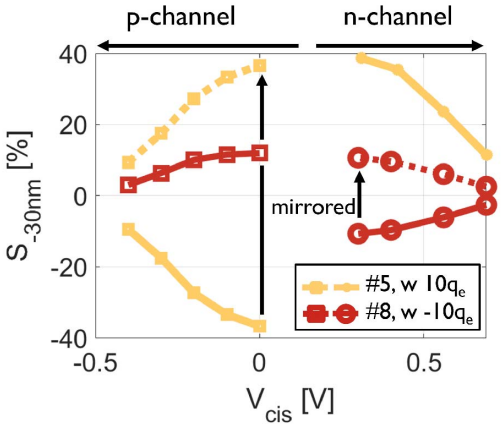

Fig. 8. Simulated sensitivity for a p-channel (left) and n-channel (right) version of architecture #5 (light color curves) and #8 (dark color curves) in the presence of respectively a positively ($10\,q_e$) and a negatively charged molecule ($-10\,q_e$) at a depth of -30 nm for $V_{cis\text{-}trans} = 80$ mV.

while other parameters remain the same. As is illustrated in App. Fig. 8, the NP-FET works both with an n-channel FET and with a p-channel FET. The rather symmetric positive sensitivity curves show that limited impact is expected from the type of FET. Note that the sensitivity of the p-channel NP-FET to a positively charged molecule has a negative value, because the current decreases upon increasing the average electrostatic potential in the pore.

Appendix D
Negatively Charged Molecule

The sensitivity of the NP-FET, with its typically negative silanol surface charge density, is dependent on the sign of the

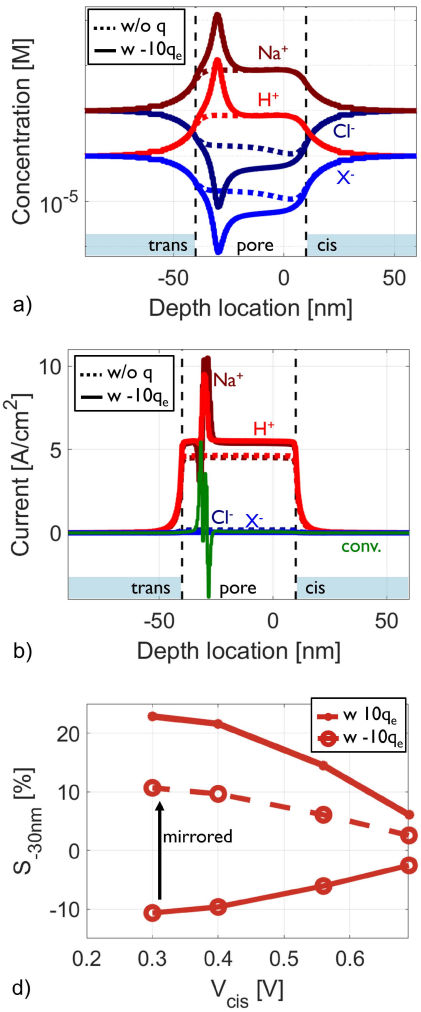

Fig. 9. Fluidic transport for architecture #8 with (solid) or without (dashed) the presence of a negatively charged molecule ($-10\,q_e$) at a depth of -30 nm for $V_{cis\text{-}trans} = 80$ mV and $V_{cis} = 400$ mV: (a) ion concentrations and (b) ion drift-diffusion current densities and total convection current density. The data correspond to the values on a straight line at 2 nm distance from the center of the pore. (c) Simulated sensitivity in the presence of a positively ($10\,q_e$) and a negatively charged molecule ($-10\,q_e$).

molecular charge. In particular, the NP-FET is more sensitive to positively charged molecules than to negatively charged molecules, as can be seen in Fig. 9.

A negatively charged molecule causes an increase in the already dominant cation concentration (see Fig. 9(a)), resulting in a modest increase in the cation ion currents (see Fig. 9(b)), while the anion and convection currents stay small. This modest increase is reflected in a more limited change of the electrostatic potential in the section of 0 nm depth to -20 nm depth than in the case of a positively charged molecule (see comparison of Fig. 4(c) and Fig. 4(d)) and hence in a more limited sensitivity to the negatively charged molecule due to a more limited impact of the resistive divider effect (see Fig. 9(c)). In fact, the sensitivity to negatively charged molecules of this particular NP-FET is almost exclusively due to the local impact of the molecular charge on

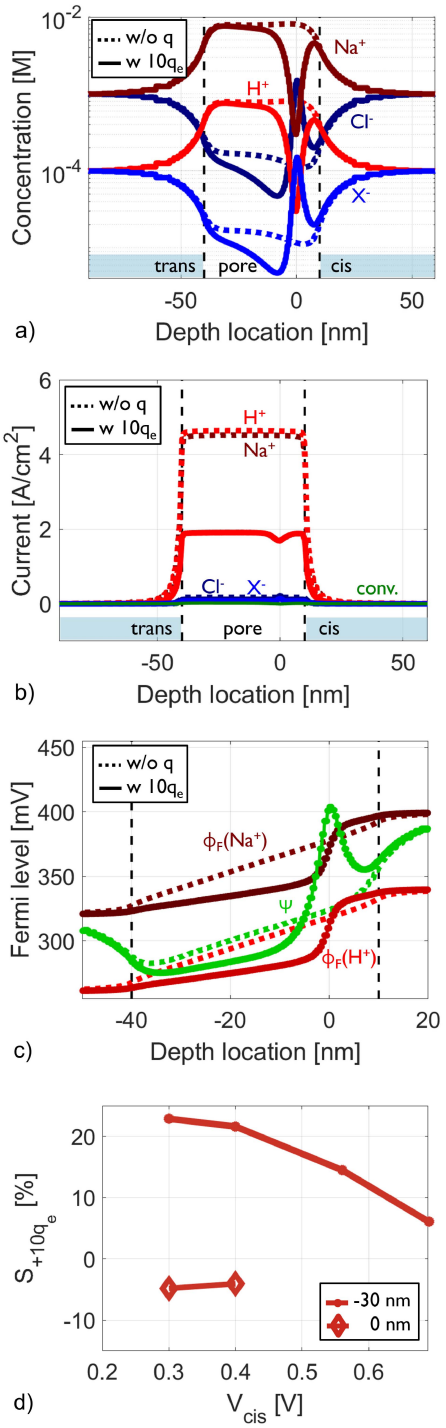

Fig. 10. Fluidic transport for architecture #8 with (solid) or without (dashed) the presence of a positively charged molecule ($10\,q_e$) at a depth of 0 nm for $V_{\text{cis-trans}} = 80$ mV and $V_{\text{cis}} = 400$ mV: (a) ion concentrations; (b) ion drift-diffusion current densities and total convection current density and (c) electrostatic (ψ) and electrochemical (ϕ_F) potential of H^+ and Na^+ with a positively charged molecule ($+10\,q_e$) at 0 nm depth. The data correspond to the values on a straight line at 2 nm distance from the center of the pore. (d) Simulated sensitivity in the presence of a positively charged molecule at a depth of -30 nm and 0 nm.

the channel of the FET. Note that the sensitivity is negative, as both the negative charge and resistive divider effect induce a more negative electrostatic potential than is present in the absence of a molecule. Further note that the impact of a neutral molecule has been partially treated before [30].

Appendix E
Molecule at the Top of the Pore

In the main manuscript, the emphasis has been on the sensitivity of the NP-FET to a molecule at the bottom of the pore, where the sensitivity is the largest. However, the sensitivity to a particle moving through the top of the pore is also non-negligible as will be discussed here.

The cation and anion concentrations change similarly to when the positively charged molecule is present near the bottom of the pore (compare Fig. 4(a) to App. Fig. 10(a)). As a consequence, also the dominant current density has a similar value compared to when the molecule is present near the bottom of the pore (compare Fig. 4(b) to App. Fig. 10(b)). The impact on the electrostatic potential is different, however. On the one hand, the large fluidic resistance at the top of the pore causes a lower electrostatic potential near the channel of the FET. On the other hand, the positive charge of the molecule tries to increase the electrostatic potential, thereby counteracting the impact of the resistive divider effect. Overall, the sensitivity for this particular example is a lowering of the effective electrostatic potential, which can be seen from the negative value of the sensitivity obtained.

The further the molecule is away from the channel, while still blocking the pore near the top of the pore, the stronger the impact of lowering the channel electrostatic potential, and hence the more negative the sensitivity will be. This is especially the case for architecture #6, for which the top oxide is thicker (30 nm), such that the FET is impacted almost exclusively by a resistive divider effect, resulting in larger values for S_{max} as a molecule passes through.

References

[1] W. E. Moerner and L. Kador, "Optical detection and spectroscopy of single molecules in a solid," *Phys. Rev. Lett.*, vol. 62, no. 21, pp. 2535–2538, May 1989.
[2] N. Akkilic, S. Geschwindner, and F. Höök, "Single-molecule biosensors: Recent advances and applications," *Biosens. Bioelectron.*, vol. 151, Mar. 2020, Art. no. 111944.
[3] P. Gross, G. Farge, E. Peterman, and G. Wuite, "Combining optical tweezers, single-molecule fluorescence microscopy, and microfluidics for studies of DNA-protein interactions," in *Methods in Enzymology*, vol. 475, N. Walter, Ed. New York, NY, USA: Academic, 2010, ch. 17, pp. 427–453.
[4] J. Zlatanova and K. van Holde, "Single-molecule biology: What is it and how does it work?" *Mol. Cell*, vol. 24, no. 3, pp. 317–329, Nov. 2006.
[5] S. Howorka and Z. Siwy, "Nanopore analytics: Sensing of single molecules," *Chem. Soc. Rev.*, vol. 38, no. 8, pp. 2360–2384, 2009.
[6] B. M. Venkatesan and R. Bashir, "Nanopore sensors for nucleic acid analysis," *Nature Nanotechnol.*, vol. 6, no. 10, pp. 615–624, Sep. 2011.
[7] D. Deamer, M. Akeson, and D. Branton, "Three decades of nanopore sequencing," *Nature Biotechnol.*, vol. 34, no. 5, pp. 518–524, 2016.
[8] D. Branton *et al.*, "The potential and challenges of nanopore sequencing," *Nature Biotechnol.*, vol. 26, no. 10, pp. 1146–1153, Oct. 2008.
[9] M. Jain, H. E. Olsen, B. Paten, and M. Akeson, "The Oxford nanopore MinION: Delivery of nanopore sequencing to the genomics community," *Genome Biol.*, vol. 17, no. 1, p. 239, Dec. 2016.
[10] R. Bowden, R. W. Davies, and A. Heger, "Sequencing of human genomes with nanopore technology," *Nature Commun.*, vol. 10, no. 1, p. 1869, 2019.
[11] K. Willems, V. Van Meervelt, C. Wloka, and G. Maglia, "Single-molecule nanopore enzymology," *Phil. Trans. Roy. Soc. B*, vol. 372, Aug. 2017, Art. no. 20160230.

[12] L. Harrington, L. T. Alexander, S. Knapp, and H. Bayley, "Single-molecule protein phosphorylation and dephosphorylation by nanopore enzymology," *ACS Nano*, vol. 13, no. 1, pp. 633–641, Jan. 2019.
[13] E. C. Yusko *et al.*, "Real-time shape approximation and fingerprinting of single proteins using a nanopore," *Nature Nanotechnol.*, vol. 12, no. 4, pp. 360–367, Apr. 2017.
[14] J. Houghtaling *et al.*, "Estimation of shape, vol. and, dipole moment of individual proteins freely transiting a synthetic nanopore," *ACS Nano*, vol. 13, pp. 5231–5242, 2019.
[15] L. Restrepo-Pérez *et al.*, "Resolving chemical modifications to a single amino acid within a peptide using a biological nanopore," *ACS Nano*, vol. 13, no. 12, pp. 13668–13676, Dec. 2019.
[16] E. A. Manrao *et al.*, "Reading DNA at single-nucleotide resolution with a mutant MspA nanopore and phi29 DNA polymerase," *Nature Biotechnol.*, vol. 30, no. 4, pp. 349–353, 2012.
[17] M. D. Peraro and F. G. van der Goot, "Pore-forming toxins: Ancient, but never really out of fashion," *Nature Rev. Microbiol.*, vol. 14, no. 2, pp. 77–92, Feb. 2016.
[18] C. Dekker, "Solid-state nanopores," *Nature Nanotechnol.*, vol. 2, pp. 209–215, Mar. 2007.
[19] L. Xue, H. Yamazaki, R. Ren, M. Wanunu, A. P. Ivanov, and J. B. Edel, "Solid-state nanopore sensors," *Nature Rev. Mater.*, vol. 5, pp. 931–951, Dec. 2020.
[20] M. Di Ventra and M. Taniguchi, "Decoding DNA, RNA and peptides with quantum tunnelling," *Nature Nanotechnol.*, vol. 11, no. 2, pp. 117–126, Feb. 2016.
[21] A. P. Ivanov *et al.*, "DNA tunneling detector embedded in a nanopore," *Nano Lett.*, vol. 11, no. 1, pp. 279–285, Jan. 2011.
[22] A. Fanget *et al.*, "Nanopore integrated nanogaps for DNA detection," *Nano Lett.*, vol. 14, no. 1, pp. 244–249, Jan. 2014.
[23] S. J. Heerema and C. Dekker, "Graphene nanodevices for DNA sequencing," *Nature Nanotechnol.*, vol. 11, no. 2, pp. 127–136, Feb. 2016.
[24] U. F. Keyser, "Enhancing nanopore sensing with DNA nanotechnology," *Nature Nanotechnol.*, vol. 11, no. 2, pp. 106–108, Feb. 2016.
[25] S. Shekar *et al.*, "Measurement of DNA translocation dynamics in a solid-state nanopore at 100 ns temporal resolution," *Nano Lett.*, vol. 16, no. 7, pp. 4483–4489, Jul. 2016.
[26] P. Xie, Q. Xiong, Y. Fang, Q. Qing, and C. M. Lieber, "Local electrical potential detection of DNA by nanowire–nanopore sensors," *Nature Nanotechnol.*, vol. 7, no. 2, pp. 119–125, Feb. 2012.
[27] B. Zhan, C. Li, J. Yang, G. Jenkins, W. Huang, and X. Dong, "Graphene field-effect transistor and its application for electronic sensing," *Small*, vol. 10, no. 20, pp. 4042–4065, 2014.
[28] W. M. Parkin and M. Drndić, "Signal and noise in FET-nanopore devices," *ACS Sensors*, vol. 3, no. 2, pp. 313–319, Feb. 2018.
[29] M. Graf, M. Lihter, D. Altus, S. Marion, and A. Radenovic, "Transverse detection of DNA using a MoS_2 nanopore," *Nano Lett.*, vol. 19, no. 12, pp. 9075–9083, Dec. 2019.
[30] D. Ruić *et al.*, "Design and modeling of a nanopore transistor," in *Proc. Int. Conf. Single-Molecule Sensors NanoSyst. (S3IC)*, 2020, pp. 194–195.
[31] X. Zhu *et al.*, "Monolithic integration of vertical thin-film transistors in nanopores for charge sensing of single biomolecules," *ACS Nano*, vol. 15, pp. 9882–9889, May 2021.
[32] S. Santermans *et al.*, "50 nm gate length FinFET biosensor & the outlook for single-molecule detection," in *IEDM Tech. Dig.*, Dec. 2020, p. 35.
[33] K. Tamersit and F. Djeffal, "Double-gate graphene nanoribbon field-effect transistor for DNA and gas sensing applications: Simulation study and sensitivity analysis," *IEEE Sensors J.*, vol. 16, no. 11, pp. 4180–4191, Jun. 2016.
[34] M. Gupta *et al.*, "Size independent pH sensitivity for ion sensitive finfets down to 10 nm width," *IEEE Sensors J.*, vol. 19, no. 16, pp. 6578–6586, Apr. 2019.
[35] *The Open Source CFD Toolbox, v. 1812*, OpenFoam, OpenCFD Ltd, Birkshire, U.K., 2018.
[36] H. G. Weller, G. Tabor, H. Jasak, and C. Fureby, "A tensorial approach to computational continuum mechanics using object-oriented techniques," *Comput. Phys.*, vol. 12, no. 6, p. 620, 1998.
[37] (2020). *Source Code of Npfetfoam*. [Online]. Available: https://gitlab.com/dinoruic/npfet_s3ic2020
[38] K. Willems *et al.*, "Accurate modeling of a biological nanopore with an extended continuum framework," *Nanoscale*, vol. 12, no. 32, p. 16775, 2020.
[39] J. Y. Song, W. Y. Choi, J. H. Park, J. D. Lee, and B.-G. Park, "Design optimization of gate-all-around (GAA) MOSFETs," *IEEE Trans. Nanotechnol.*, vol. 5, no. 3, pp. 186–191, May 2006.
[40] S. S. Sharma and P. Kumar, "Optimizing effective channel length to minimize short channel effects in sub-50 nm single/double gate SOI MOSFETs," *J. Semicond. Technol. Sci.*, vol. 8, no. 2, p. 170, 2008.
[41] U. E. Avci, D. H. Morris, and I. A. Young, "Tunnel field-effect transistors: Prospects and challenges," *IEEE J. Electron Devices Soc.*, vol. 3, no. 3, pp. 88–95, May 2015.
[42] D. Verreck, G. Groeseneken, and A. S. Verhulst, "The tunnel field-effect transistor," in *Wiley Encyclopedia of Electrical and Electronics Engineering*. Hoboken, NJ, USA: Wiley, Nov. 2016, pp. 1–24.
[43] S.-C. Chang, U. E. Avci, D. E. Nikonov, and I. A. Young, "A thermodynamic perspective of negative-capacitance field-effect transistors," *IEEE J. Explor. Solid-State Computat. Devices Circuits*, vol. 3, pp. 56–64, 2017.
[44] P. A. Farrell and E. C. Gartland, "On the scharfetter-gummel discretization for drift-diffusion continuity equations," in *Computational Methods for Boundary and Interior Layers in Several Dimensions*, J. Miller, Ed. Dublin, Ireland: Boole Press, Jan. 1991, pp. 51–79.
[45] R. E. Thomas, "Carrier mobilities in silicon empirically related to doping and field," *Proc. IEEE*, vol. 55, no. 12, pp. 2192–2193, Dec. 1967.

Anne S. Verhulst received the M.S. degree in electrical engineering from KU Leuven, Belgium, in 1998, and the Ph.D. degree in electrical engineering from Stanford University, USA, in 2004. She joined imec, Belgium, in 2005. Since October 2021, she is also an Honorary Visiting Assistant Professor with the Electrical Engineering Department, KU Leuven. Her research interests include modeling, calibration and fabrication of tunnel field-effect transistors, and modeling and calibration of the dynamics of ferroelectric switching. More recently, she is focusing on projects merging nano-electronics with life sciences.

Dino Ruić received the M.S. degree in physics from the University of Bonn, in 2011, and the Ph.D. degree from RWTH Aachen University, in 2017. He was with imec, Belgium, from 2017 to 2019, and thereafter joined Alphabet's X, California. His research interests include semiconductor devices, biosensors, electronic circuits, and numerical methods for partial differential equations.

Kherim Willems received the B.S. and M.S. degrees in biochemistry and biotechnology from KU Leuven in 2012, and the Ph.D. degree in physics from KU Leuven in 2021. For his work on the computational modeling of biological nanopores. Since 2018, he has been working at imec, Belgium, as a Researcher. His current research interests include investigating novel nanopore technologies for (bio)sensing, developing next-generation memories, and understanding the physics of nanoscale transport. His research expertise covers both experimental and theoretical approaches.

Pol Van Dorpe received the Ph.D. degree from the Faculty of Engineering, KU Leuven, in 2006. Afterwards he was appointed as a Postdoctoral Fellow of the FWO-Flanders (2006–2012), based in imec, and focused onmetal-based nanophotonics or plasmonics for biosensors and energy harvesting. He is currently an imec Fellow of the Life Science Technologies Department, imec, Belgium, where he leads a team working on photonic and nanopore technology for life science applications. Since 2012, he has been holding a position as a part-time associate professor with the Physics Department, KU Leuven. His work has led to over 150 peer-reviewed articles in high-impact-factor journals and has attracted more than 7000 citations.